Fully integrated entangled photon-pair source on a photonic chip for a wavelength-multiplexed multiparty quantum key distribution network

Maximilian Mengler, Jakob Kaltwasser, Erik Fitzke, Thomas Hoffmann, and Thomas Walther*
Institute for Applied Physics, Technische Universität Darmstadt, Schlossgartenstraße 7, 64289 Darmstadt, Germany

(Received 5 September 2025; accepted 19 October 2026; published 13 November 2026)

The development of QKD networks as a possible answer to the threat to encrypted communication posed by quantum computers has given rise to a variety of concepts and implementations in recent years. In terms of the scalability of such systems, photonic integrated circuits (photonic chips) are a promising approach. This makes the systems not only much more miniaturized and robust, but also more attractive for industrial production. Here we present the concept and characterization of a photonic chip that can act as a source in an entanglement-based QKD network employing spontaneous four-wave mixing in microring resonators. In addition to photon-pair production, the chip also directly performs essential filtering tasks. Moreover, the photon-pair rate can be maintained constant over an extended period using a Pound-Drever-Hall locking method.

DOI: 10.1103/n4rw-wgx1

I. INTRODUCTION

Entangled photon-pair sources are valuable resources in multiple research areas such as quantum key distribution (QKD) [1,2] and quantum computing [3]. They can act as heralded single-photon sources or provide entangled quantum states [4,5].

Depending on the application, various techniques are commonly employed for their construction. For example, PPLN [6,7] or PPKTP [8,9] nonlinear crystals enable the generation of photon pairs via spontaneous parametric down-conversion (SPDC).

Another promising way of constructing such sources lies in photonic integrated circuits (PICs) based on silicon nitride waveguides. The material's high third-order nonlinearity enables photon-pair generation via spontaneous four-wave mixing (SFWM) at wavelengths around 1550 nm [10,11]. The general validity of such sources has been shown on several occasions [2,4,12]. Besides silicon nitride, which benefits from very low propagation losses, also other PIC platforms, like silicon, silicon carbide, or AlGaAs, are candidates for realizing photon-pair sources [13–15].

The use of PICs shows several advantages when compared to conventional sources. These range from more compact devices easily shieldable from environmental influences, to better scalability in industrial mass production, as well as the combination with various other components on the same device [16]. SFWM, as the driving effect of the photon-pair generation, allows the use of a pump laser at the same wavelength as the photon pairs.

In addition to various QKD protocols that can be implemented on photonic chips, such as CV-QKD [17], chips also offer the possibility of accommodating most optical components. Lasers [18–20], demultiplexing on chips [21–23], interferometers on chips [24–26], and single-photon detectors on chips [27,28] are all possible in principle and are the subject of current research. This means that photonic chips will offer the possibility of implementing the entire optical setup on one or more chips in the future. First steps in this direction have been already presented [29].

In the following, we present a concept for a PIC design combining several functionalities of a photon-pair source into a single system. We show its advantages with results obtained from a chip in our laboratory. On the chip, we generate photon pairs via SFWM inside microring resonators. This enhances the efficiency of pair production and makes pairs to occur at a frequency comb matched to the ITU grid, enabling the easy separation of entangled photons using commercially available equipment.

Furthermore, we incorporated several filtering stages directly on the chip, drastically reducing noise generated by Raman scattering. With external filters only, additional noise photons would be generated between the filters and the photon-pair production itself.

Due to the high-temperature dependence of the waveguides' refractive index, a resonator's resonance position becomes unstable even in a laboratory environment. Thus, we adapted the PDH locking scheme for our pulsed setup and actively stabilized the resonance frequency of the microrings to the pump light.

We then present a general characterization of the chip, focusing on its filtering capabilities and its potential as a photon-pair source, and subsequently incorporate it into our existing QKD setup, enabling the exchange of secure quantum keys.

*Contact author: thomas.walther@physik.tu-darmstadt.de

Published by the American Physical Society under the terms of the Creative Commons Attribution 4.0 International license. Further distribution of this work must maintain attribution to the author(s) and the published article's title, journal citation, and DOI.

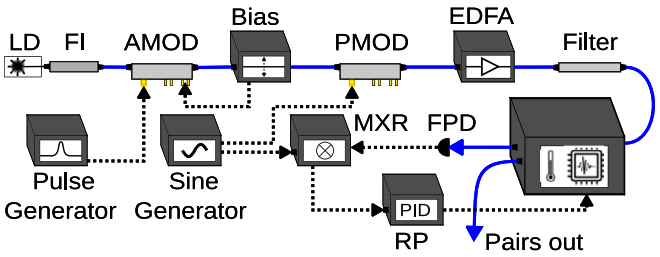


FIG. 1. Schematics of the general setup surrounding the chip. The chip itself is placed inside a temperature-stabilized box. Fibers are marked solid blue, and electrical lines are dotted black. LD: laser diode; FI: fiber isolator; AMOD: amplitude modulator; PMOD: phase modulator; EDFA: erbium-doped fiber amplifier; FPD: fast photodiode; MXR: mixer; RP: RedPitaya.

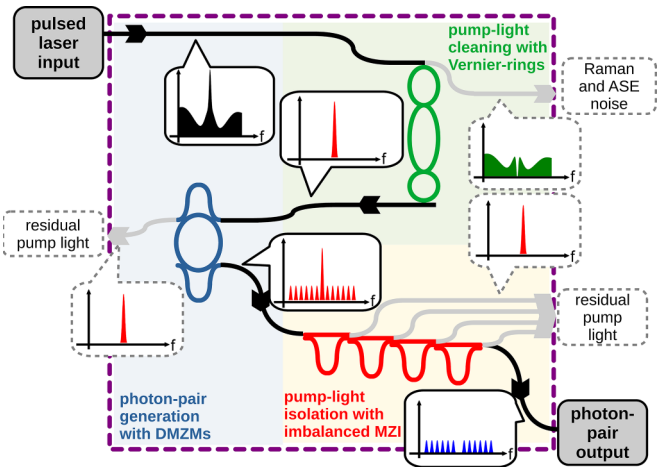


FIG. 2. Sketch of the chip design and its concept. Externally created pulsed pump light is guided to the chip (purple box), where three tasks are performed: First, the laser line is cleaned on-chip with a Vernier ring. Subsequently, the cleaned pump light is used in a dual Mach-Zehnder microring (DMZM) [37–39] or a simple microring resonator for photon-pair generation. Afterwards, the remaining pump light is filtered by a series of asymmetric Mach-Zehnder interferometers (AMZIs).

II. SETUP

The completely fiber-based setup is depicted in Fig. 1. Pump light is generated by a DFB laser diode tuned to 193.35 THz. This frequency lies at the edge of two ITU channels in the center of the optical C-Band, which is widely used for fiber-based telecommunication. The light is emitted linearly polarized in a single transversal mode, for which the chip is optimized. The continuous light is shaped into pulses of variable length and repetition rate with an amplitude modulator to match the requirements in our time-bin QKD implementation. The power may be decreased with a variable optical attenuator or increased with an erbium-doped fiber amplifier.

The chip is placed inside a temperature-stabilized box shielding it from the environment, keeping its temperature stable within a range of 2 mK. Otherwise, temperature fluctuations could change the optical path length of the chip's waveguides and, therefore, deteriorate its alignment.

A. Photonic chip concept and design

The PIC is designed as an all-in-one solution for photon-pair generation and filtering with several redundancies for testing purposes. The chip's conceptual design is depicted in Fig. 2. Not included in the figure, several components on the chip were manufactured in multiple variations, interchangeable via interferometers used as optical switches. The main purpose of photon-pair generation is enabled by the chip platform of silicon nitride, allowing spontaneous four-wave mixing. The chip was produced by Lionix International in the TriPlex geometry utilizing asymmetric double-stripe waveguides [30].

Light traveling through optical fibers always generates a spectral background due to nonlinear effects, e.g., spontaneous Raman scattering (SRS) [5,31]. If left unchecked, such a background will mix with created photon pairs and become indistinguishable from them. Thus, the first component on the chip is used for spectral filtering and consists of several ring resonators coupled in a row between two waveguides [32]. These special ring filters were designed to transmit a narrow band around the laser line but to suppress any background around it. They were placed directly in front of the photon-pair generation stage, so only a minimum of noise is generated after filtering. We implemented two interchangeable sets of filters: Two serially coupled rings with FSRs of 60 GHz and 56 GHz, and three serially coupled ring resonators with FSRs of 75 GHz, 45 GHz, and 70 GHz. To predict the filters' behavior, we calculated their frequency response functions depending on the FSRs and coupling coefficients [33,34]. We chose these parameters so that the spectrum transmitted through the filters includes a broad plateau (≈3 GHz) around the pump frequency, making the transmission both more stable and allowing for the sidebands introduced for the PDH locking to pass through the filter unattenuated.

The photon pairs are then generated inside simple single-bus ring resonators [35,36] or dual Mach-Zehnder microrings (DMZM) [37–39]. As a third-order nonlinear process, SFWM is quadratically dependent on the pump power and gains efficiency inside the resonators, where the power is enhanced due to critical coupling. The photon pairs generated via SFWM then emerge in a frequency comb matching the resonators' free spectral range (FSR). The FSR is set to 50 GHz, ensuring that half the generated photon pairs match the centers of ITU-grid channels [40,41]. The linewidths are expected around 200 MHz to 400 MHz and the FSRs of the DMZMs' MZIs are set to 100 GHz. Thus, the photon pairs in the center of ITU channels can be guided directly into a separate bus from the pump light and other noise photons, and may be extracted with an individual coupling coefficient.

After the photon-pair generation, those photons matching the centers of ITU channels have to be separated from ones at the edges, as well as the remaining pump light. This is especially the case for the simple ring resonators, but it is also necessary for the DMZMs to a lesser extent. For this purpose, we placed filters in the form of ring resonators and asymmetric Mach-Zehnder interferometers (AMZIs) directly behind the

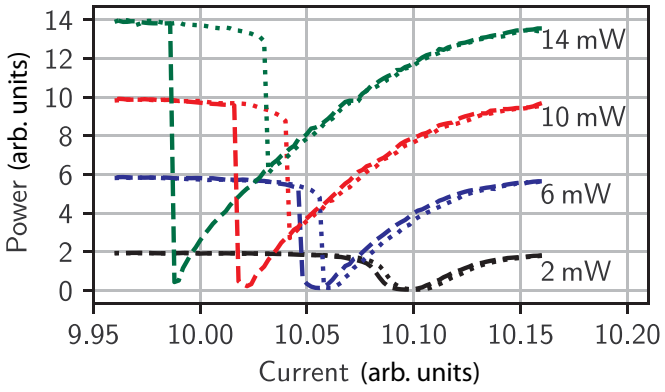


FIG. 3. Transmission past a ring resonator at 193.35 THz for different input powers, depending on the current applied to the ring's heating element. The lines were recorded in both sweeping directions with increasing (dotted) and decreasing (dashed) currents.

SFWM-stage. All the filters were designed with an FSR of 100 GHz.

While it is important for the filters before the photon pair generation to have only a narrow passband and to filter out as much light as possible close to the pump frequency using the largest possible FSR, it is sufficient–and even mandatory–for the pump light filter to filter only the narrow frequency band around the pump frequency. A large FSR is not needed, which is why interferometers were chosen for filtering here. In contrast to the Vernier rings before photon pair generation, they have the advantage of being much less sensitive to temperature and thus phase changes making them more stable and easier to adjust.

All of the resonators and interferometers on the chip are equipped with electrical heating elements placed above their waveguides. This enables the manipulation of optical path lengths and, thus, the adjustment of the components.

B. PDH locking

The PDH technique [42–44] is implemented to lock the resonance frequency of the ring used for photon-pair production to the pump light. The necessity for some locking mechanism arises from shifts in the resonance position due to even small changes in the external temperature and due to self-heating effects [45,46] that arise from light circulating inside the resonator. As seen in Fig. 3, especially at higher pump powers, the shape and position of the resonances are influenced. The flank at lower heating currents can become very steep, and a minor instability may result in a significant change in the resonance condition. Furthermore, a hysteresis effect becomes observable, as the shape of the resonance depends on the direction in which the current is varied.

The PDH setup starts with a dual-channel signal generator that emits sinusoidal electrical signals at around 1.5 GHz. The signal from the first channel is routed to an optical phase modulator in front of the PIC to create sidebands in the pump light. The signal from the second channel with an adjustable phase shift is routed to one input of an analog mixer, as common digital components wouldn't be able to handle the high frequencies involved. The mixer's other input originates from a fast photodiode that measures part of the residual pump light after it passes the resonator and exits the chip.

The signal generated by the mixer is guided to a RedPitaya StemLab used as a PID controller. The resulting signal is routed through a self-built current-reducing circuit inserted into the circuit powering the heating element above the stabilized resonator. Thus, it is possible to directly adjust the current passing through the heating element dependent on the PID signal.

III. PULSED PDH LOCKING

With the PDH technique ordinarily used to stabilize continuous wave (CW) lasers to a resonator, we present an adaptation to work with pulsed light. This is necessary, e.g., for time-bin QKD protocols. Here we present the results of analytical calculations, giving direct insight into the effects of different parameters on the error signal. The calculations are presented in the Appendix in more detail.

The linewidth of the CW diode laser in our setup is much below 1 MHz, which is negligible compared to the frequency shifts introduced by the modulators in the range of hundreds of megahertz, such that the CW laser light is well approximated as $E_{\mathrm{in}}(t) = E_0 \exp(-\mathrm{i}\omega_0 t)$. The effects of the amplitude and phase modulation are modeled by multiplying with the functions $M_{\mathrm{A}}(t)$ and $M_{\mathrm{P}}(t)$:

$$M_{\mathrm{A}}(t) = \sum_{k=-\infty}^{\infty} \alpha(t - kT) = \sum_{j=-\infty}^{\infty} a_j \mathrm{e}^{-\mathrm{i}j\omega_{\mathrm{AM}}t}, \tag{1}$$

$$M_{\mathrm{P},j}(t) = \exp\{-\mathrm{i}[\varphi_{0,j} + 2h_j \sin(\omega_{\mathrm{PM}}t)]\} \tag{2}$$

$$= \sum_{m=-\infty}^{\infty} b_{m,j} \mathrm{e}^{-\mathrm{i}m\omega_{\mathrm{PM}}t}. \tag{3}$$

Here $\alpha(t)$ is the pulse envelope repeated with period $T = 2\pi/\omega_{\mathrm{AM}}$ and the $a_j = \int_{-T/2}^{T/2} \alpha(t)\mathrm{e}^{\mathrm{i}j\omega_{\mathrm{AM}}t}\,\mathrm{d}t/T$ are its Fourier coefficients. The Jacobi-Anger expansion [47] yields the coefficients $b_{m,j} = \mathrm{e}^{-\mathrm{i}\varphi_{0,j}} J_m(h_j/2)$ with the Bessel functions of the first kind J_m. The modulation index h and phase φ_0 depend on properties of the traveling-wave modulator such as the attenuation and phase velocity mismatch of the optical and electrical fields [48]. They are, in general, different according to optical input frequencies labeled with j.

Together with the frequency response function $\tilde{F}(\omega, \Phi)$ of our resonator the error signal $\epsilon(\Phi, \vartheta)$, dependent on the phase Φ within the resonator and the phase delay ϑ of the demodulation signal, can be derived following the calculations shown in the Appendix:

$$\begin{aligned}\epsilon(\Phi, \vartheta) = 2\pi |E_0|^2 h \sum_{\substack{m,m'=-\infty \\ j,j'=-\infty}}^{\infty} \mathrm{Im}\Big(& a_j a_{j'}^* b_m b_{m'}^* \mathrm{e}^{\mathrm{i}\vartheta} \\ & \times \tilde{F}(\omega_0 + m\omega_{\mathrm{PM}} + j\omega_{\mathrm{AM}}, \Phi) \\ & \times \tilde{F}^*[\omega_0 + (m-1)\omega_{\mathrm{PM}} + j\omega_{\mathrm{AM}}, \Phi] \\ & \times \delta[(m - m' - 1)\omega_{\mathrm{PM}} + (j - j')\omega_{\mathrm{AM}}]\Big).\end{aligned} \tag{4}$$

With a small modulation amplitude h, most of the light remains in the central band and only a small portion is

transferred to the first-order sidebands. Higher orders are then negligible and only the indices $m = -1, 0, 1$ are relevant in the experiment. Note that the δ function represents a low-pass filter in the experimental setup, which should be set so that all the possible nonzero sums of frequencies $(m - m' - 1)\omega_{\mathrm{PM}} + (j - j')\omega_{\mathrm{AM}}$ are filtered out.

The resulting error signal comprises three parts. First, the part where $j = j' = 0$ follows the same course as the error signal without amplitude modulation. The second part, where $j = j' \neq 0$, follows the same course for every j, but is shifted by $j\omega_{\mathrm{AM}}/\mathrm{FSR}$. The total sum over these cases can be regarded as a convolution of the initial error signal with the pulse shape in the frequency domain. This convolution results in an error signal with less sharp curves, but does not prevent its use for pulse forms typically used.

A possible third part due to the amplitude modulation can arise when the condition $(m - m' - 1)\omega_{\mathrm{PM}} + (j - j')\omega_{\mathrm{AM}} = 0$ is fulfilled without $j = j'$. For greater values of m, m', j, and j', these influences become rather small as the corresponding coefficients generally decrease in their absolute value with greater indices. It is, however, possible for significant distortions of the error signal to occur provided the condition is fulfilled for smaller index values. This is especially the case if the phase modulation frequency ω_{PM} is a multiple of the amplitude modulation frequency ω_{AM}. Therefore, it is preferable to choose an ω_{PM} that differs from multiples of the amplitude modulation. Also, it is noteworthy that the effect of the amplitude modulation becomes greater with shorter pulses, as there are more coefficients a_j of relevant magnitude in this case.

To suppress undesired influence from the first order while keeping the low-pass filter at maximum frequency, the phase modulation is chosen to fulfill the following condition:

$$\omega_{\mathrm{PM}} = \left(n + \tfrac{1}{2}\right)\omega_{\mathrm{AM}}, \quad n \in \mathbf{N}. \tag{5}$$

This ensures that occurring beat notes assume their maximum value of $\omega_{\mathrm{AM}}/2$. Given the case that low-pass filters with lower cutoff frequencies are available, and higher orders of m need to be considered, a different condition may be chosen.

For the parameters chosen for the experiments presented in the following, we chose the following:

(1) A pulse width of 10 ns so that the resonators get fully loaded by each pulse.

(2) A repetition rate of 10 MHz resulting in moderate photon rates at our SPDs.

(3) A phase modulation frequency of 1.505 GHz exceeding the linewidth of our ring resonators.

IV. RESULTS

In the following, we present the results of the characteristic measurements for the PIC. Initial results of the chip as a photon-pair source in an entanglement-based two-party QKD system are also presented and analyzed.

A. Filters

The performance of the filtering units was investigated in two modes. First, we examined the single-photon spectrum emitted by the PIC with and without on-chip filters in use. We placed external filters fulfilling the same function in front of and behind the chip with around 2 m of fiber in between. No ring for photon-pair production was tuned to resonance. The resulting spectra are depicted in Fig. 4. There the initial filter for background removal comprised three rings, and four filters consisting of a single ring each were used for pump suppression afterwards. In the figure it is obvious that both filtering units have a significant effect on the reduction of noise present behind the chip. There is also a peak visible around the pump frequency, which is addressed in Sec. IV B.

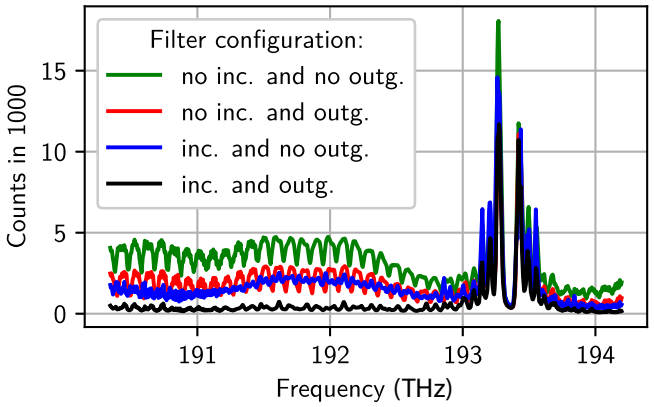


FIG. 4. Single-photon spectra with and without on-chip filters in use. Pump cleaning (inc.): three-ring filter; pump suppression (outg.): four single-ring filters.

Further measurements have shown that the initial filters consisting of three rings exhibit a better extinction ratio than those with only two, but those are also able to significantly reduce the amount of noise. Between AMZIs and ring resonators used for pump suppression, we found no significant difference with regard to the noise suppression.

However, we also investigated the filters regarding their ability to suppress the pump light and separate it from the pairs. Thus, the pump laser was guided to the beginning of a filtering block, and the power transmitted by the block when all the subfilters were adjusted to maximal transmission of the pump light compared with the power when one or more subfilters were adjusted towards filtering operation. For each setup, two suppression values were taken: one ideal value, where the regarded subfilter was optimally adjusted, and an estimation for an effective value that accounts for fluctuations in the adjustment during ordinary operation without constant filter readjustment.

These measurements yielded maximum suppression rates for the single ring filters of 30 dB to 39 dB while effective values were estimated between 24 dB and 34 dB. For the AMZIs, the maximal suppression rates were measured with 21 dB while the realistic estimations were only half a decibel below that. However, we found a dependence of the AMZIs' performance on the exit ports allocated to the photon pairs and residual pump light. If the photon pairs' exit port lies on the same waveguide as the input port, the pump suppression was shown to be inferior to the switched case. This is most likely due to slight systematic deviations in the coupling coefficient

of the 50/50 couplers from their specified values, caused by fabrication imperfections.

Then, the pump light's destructive interference happens between two fields that do not have the same amplitude, as one was reflected twice while the other was transmitted. Due to this deviation, the destructive interference will always leave some residual light behind. By contrast, if the photon pairs are directed to the exit port on the opposite waveguide, the destructive interference of the pump light occurs between two nearly equal fields. These fields were both initially reflected and subsequently transmitted, resulting in a significantly reduced amount of residual light. Then, the maximal suppression ratios of the MZIs were determined between 51 dB and 61 dB, while effective values were estimated around 40 dB.

In addition to the single filters, cascaded filters were also investigated and it was found that a sequence of ring filters demonstrated a deterioration in the effectiveness of additional rings. With the suppression of the first ring at 39 dB, the second ring yielded an additional suppression of only 11 dB. The combination of four rings showed an overall pump suppression of 53 dB. By contrast, the MZI filters showed a far better performance in cascaded operation. With two combined MZIs, each one individually delivered a pump suppression of 21 dB. The combination of four filters yielded a total suppression of at least 67 dB exceeding the resolution of our measurement setup. We assume that the inferior performance of the rings in this case originates from light that couples out of the rings, where the power is enhanced, and couples back into the waveguide with the photon pairs.

In an additional measurement, we checked whether the AMZI-based pump suppression filters were able to reduce the pump light below the level of the generated photon pairs and found that this is not the case. However, we are confident that the filters' performance will be sufficient when their exit ports are switched.

B. Single-photon spectrum

The single-photon spectrum measured with a Czerny-Turner-type spectrograph for a single-bus ring and for a short waveguide without any further components on the chip is shown in Fig. 5. The single-bus ring was not in resonance for this measurement. So the amount of photons generated inside the rings should be negligible, but a significant amount of the background is extinguished at the resonance positions visible through dips in the spectrum.

Towards the edges of the spectrum, one can see the rising of plateaus caused by spontaneous Raman scattering (SRS) occurring several THz distant from the pump light in glass fibers and silicon nitride [5,31,49]. The effect is widely known and diminishes the CAR only in the outer reaches of the spectrum. In addition, the noise that originates before the photon-pair generation components can be filtered as seen in Sec. IV A.

In the central part of the spectrum, close to the pump frequency, the phase-matching condition of the SFWM process is maximally fulfilled. Hence, the photon pairs should be generated there most efficiently. However, we found that the peak in the center is mainly not created by SFWM but by a yet unknown nonlinear effect that creates single photons. With these peaks only occurring when the chip is part of the setup, we rule out the possibility that it is generated outside of the PIC. Coincidence measurements show that the coincidental over accidental ratio (CAR) in this spectral region is very low, indicating a high amount of uncorrelated photons rather than the expected correlated photon-pairs from SFWM.

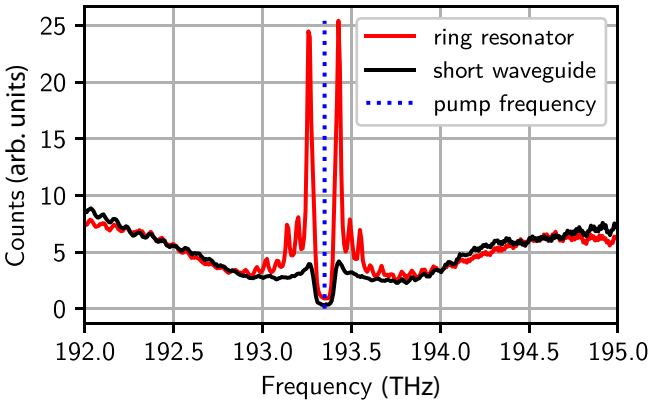


FIG. 5. Single-photon spectra of an off-resonance single-bus ring resonator (red) and a short waveguide (black). The spectra were generated with a 15 mW cw laser at 1550.5 nm and a 180 s measurement with a Czerny-Turner-type spectrograph. Additional fiber-based filter elements before and after the chip were used to spectrally clean the pump light and separate the single photons from the laser light. Note that the difference in amplitude between the signals is not caused by the ring resonator, as it is off-resonance, but by the different waveguide length.

We were not able to identify the effect causing the noise with comparable results in literature: The maximum of SRS occurs at higher frequency offsets, at about 3 THz from the pump [5,31], and spontaneous Brillouin scattering occurs at lower frequency offsets, at about 10 GHz from the pump [50]. Probably the same effect has previously been reported in [51–53], in both silicon and silicon nitride, but the root cause was not identified. Only the suspicion was raised that some kind of scattering with thermal excitations is responsible.

We observed the effect on our chip with asymmetrical double-stripe waveguides from LioniX and also on chips with symmetrical double-stripe waveguides from LioniX. However, in a chip with boxed waveguides, also from LioniX, we were not able to reproduce the effect. Since the boxed waveguide geometry also has a different dispersion coefficient, a correlation between dispersion and the noise generation is possible, but has not yet been verified.

We have characterized the effect as linearly dependent on the waveguide length and pump power. The created single photons have no measurable offset to the pump light in time, ruling out fluorescence (detector jitter below 200 ps). Within the range of 193.05 THz to 193.55 THz available to us there was also no dependence on frequency of the pump laser observable. The same holds true for the efficiency of the nonlinear effect due to detuning of the laser frequency in this range or the spectral shape or its efficiency peak at about 90 GHz from the laser frequency.

As the generated noise significantly overlaps with the photon pairs generated by SFWM, the effectiveness of our

source is drastically reduced. The problem cannot be solved effectively because the phase-matching spectrum is quite narrow-banded, given the high dispersion of 1117 $ps^2\,km^{-1}$ in the asymmetric double-stripe waveguides on the TriPlex platform. Hence, there is very little SFWM efficiency outside the bandwidth of the unexplored noise effect. Therefore, the effective efficiency of photon-pair generation on the chip is reduced.

C. Photon-pair generation

To avoid the noisiest regions of the single-photon spectrum presented above, the photon-pair production was investigated about 450 GHz distant from the pump frequency. The photon-pairs were separated with an AWG and sent to individual single-photon detectors (IDQubes from ID Quantique). The arrival times of the detected photons were stored with a time-tagging unit (ID900 from ID Quantique).

Because the detectors were operated with a finite dead time of 10 µs and afterpulsing a relevant factor, photon arrival rates could not be deduced directly from the generated files. Different approaches to handling such effects have been introduced [54,55]. We chose to apply a postselection scheme, which we previously presented in [7,56]. To exclude coincidences caused by uncorrelated photons, we determined the coincidence rate both for the ordinary timestamp lists and for the case with one shifted by one repetition cycle, and subtracted the latter rate from the former.

The count rates were then inserted into a simple model similar to one presented in [5], allowing the calculation of photon-pair generation rates and detection efficiencies. The power-dependent single count rates $R^{(i)}(p)$ $(i = 1, 2)$ and coincidental count rates $R_c(p)$ then follow:

$$R_c(p) = \eta^{(1)}\eta^{(2)} D \epsilon_2 p^2 = a_c p^2, \tag{6}$$

$$R^{(i)}(p) = \eta^{(i)} D(\epsilon_1^{(i)} p + \epsilon_2 p^2) + R_d^{(i)} = a_i p^2 + b_i p + R_d^{(i)}. \tag{7}$$

Here $\eta^{(i)}$ describes the detection efficiency in the corresponding channel, D the duty cycle of the driving pulses, ϵ_2 the photon-pair generation, $\epsilon_1^{(i)}$ the noise photon generation, and $R_d^{(i)}$ the dark count rate in channel i.

Coincidence measurements were then performed with the single-bus ring and DMZMs with the deepest resonances, indicating critical coupling and thus the highest expected photon-pair generation rate. These measurements were performed with rectangular pulsed pump-light with a repetition rate of 10 MHz and a pulse width of 10 ns. Different measurements were performed with peak powers up to 130 mW. By fitting quadratic functions to the resulting coincidence rates and second-order polynomials to the single rates, the coefficients a_c, a_i, and b_i could be extracted from the data. These allowed the determination of the other remaining parameters:

$$\eta^{(1)} = \frac{a_c}{a_2},\ \eta^{(2)} = \frac{a_c}{a_1},\ \epsilon_1^{(i)} = \frac{b_i}{\eta^{(i)} D},\ \epsilon_2 = \frac{a_c}{\eta^{(1)}\eta^{(2)} D}. \tag{8}$$

The values obtained for the efficiencies and generation rates can be inspected in Fig. 6. The relatively low detection efficiencies in the area of 2% to 3% are for the most part caused by the detectors with an efficiency of 25% and a subpar AWG with an insertion loss of 6 dB. Thus, the outcoupling efficiency of the photon pairs from the resonators and chip can be estimated in the area of 30% to 60% depending on the resonator, which lies in the expected regime.

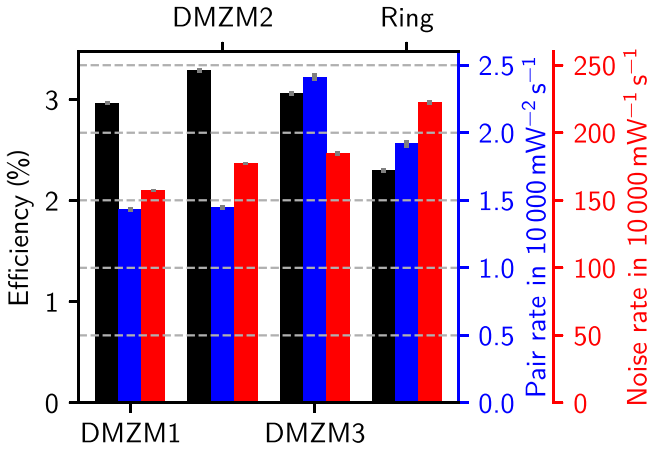


FIG. 6. Detection efficiencies and generation rates corresponding to four resonators. The pump light was pulsed with 10 ns pulse width and 10 MHz repetition rate. Photon generation rates are referenced to the peak power and divided by the duty cycle.

Furthermore, the power-dependent coincidental over accidental ratio (CAR) was determined by comparing the correlated and uncorrelated coincidences. It is shown in Fig. 7 for the different resonators at different powers. Therein we also compare the maximum CAR for a coincidence window of 100 ps and the one reached at 2 ns also used to determine the PGRs. For every resonator, the CAR decreases for higher pump powers, which we attribute to an increase in accidental coincidences with noise photons for the most part. The CAR also decreases dramatically with the longer coincidence window, which is a trade-off for a higher effective detection efficiency.

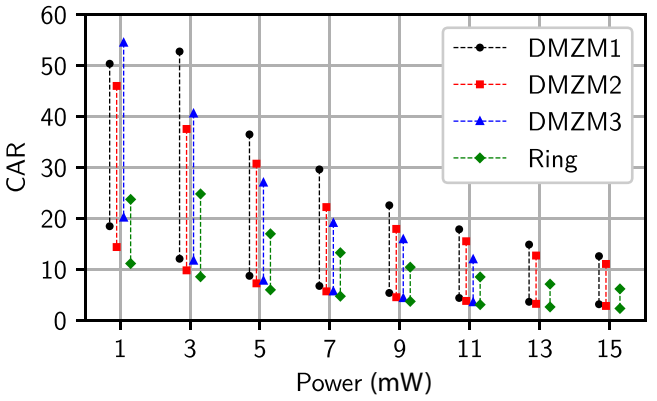


FIG. 7. CAR for different rings and average pump powers with 10 ns pulse width and 10 MHz repetition rate. The points that appear in a group were measured at the same power in the center of that group. The higher values represent the maximum CAR with a coincidence window of 100 ps and the lower ones for a coincidence window of 2 ns.

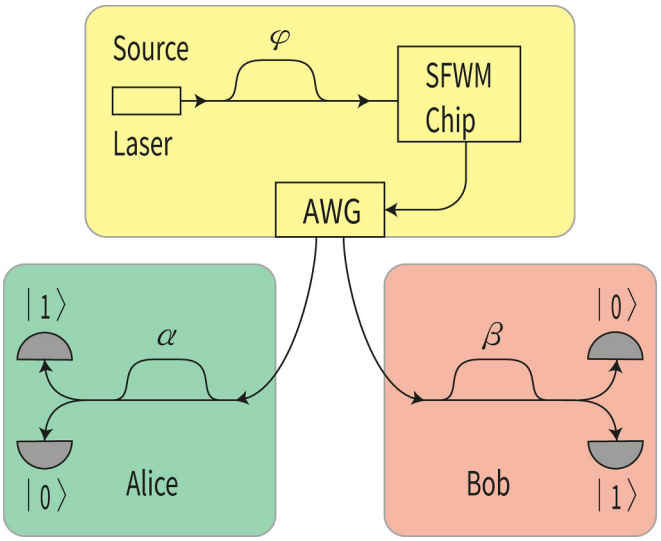


FIG. 8. Overview of the BBM92-based QKD setup using SFWM on the photonic chip as photon-pair source. The created photon pairs are split with an arrayed waveguide grating (AWG). According to the BBM92 [1] protocol, the phases of the interferometers α, β, φ are adjusted to each other.

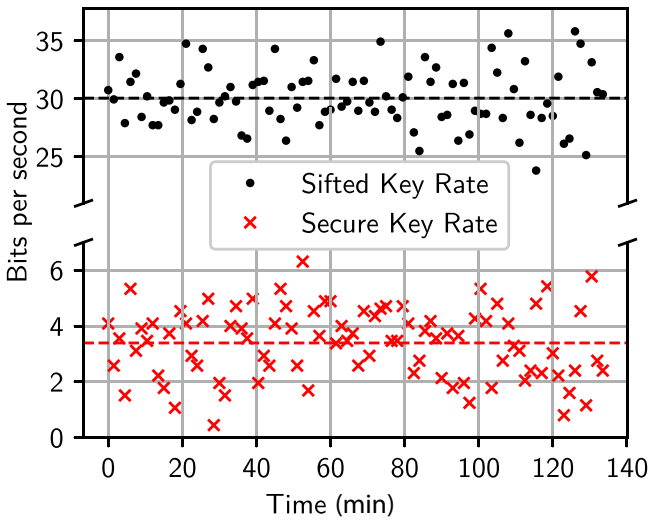


FIG. 9. Sifted and secure key rates from a two-hour QKD measurement using the chip as the photon-pair source. After each iteration of 90 s, the QBERs are evaluated and a key is obtained. The dotted lines indicate the average key rates.

D. Quantum key distribution

Although the previous measurements revealed a nonideal behavior of the PIC, its use for QKD is still viable. Thus, we performed QKD experiments replacing the photon-pair source in our preexisting setup [57–59] with the PIC. It implements the entanglement-based BBM92 protocol [1] with phase-time coding. The schematic setup is depicted in Fig. 8.

A major difference introduced by the photonic chip replacing our previously used SPDC source is a minimum value for the pulse lengths of about 5 ns corresponding to the linewidth of our resonators of approximately 200 MHz. With lower pump pulse lengths (higher spectral width of the pump light), the power circulating inside the resonators, and thus the photon-pair production, will not reach its maximum. For higher Q factors of the ring this effect increases, but higher Q factors also ensure a higher photon-pair production efficiency. The interferometers used in our QKD setup were chosen with a delay of 18.36 ns exceeding the minimum pulse length by far. Our experiments show that for constant pump power, the QBER increases with pump pulses longer than 5 ns. Therefore the minimum effective pulse length of 5 ns has been chosen for the following measurements.

On chip, the incoming pump light was filtered with a triple-ring before entering DMZM3, where the SFWM photon-pair production took place. DMZM3 was chosen for its relatively high photon-pair production efficiency and outcoupling efficiency. After the resonator, the residual pump light and the created photon pairs were separated with a series of 5 AMZIs, and the remaining photon pairs were distributed with an arrayed waveguide grating (AWG). AMZIs were used as pump filters, in accordance with the results presented in Sec. IV A.

In the trade-off between higher noise close to the pump frequency and lower phase matching of the SFWM-process farther away, the frequency pair of 192.9 THz and 193.8 THz was chosen for Alice and Bob in the QKD setup, i.e., the same that were used for the coincidence measurements in Sec. IV C.

The pulsed PDH locking proved to be stable in the QKD-source setup up to 12 mW medium pump power. For the QKD measurements, an average pump power of 7 mW was used at an optimum for the combination of photon-pair count rates and the time QBER. This pump power was used in combination with a pulse length of 5 ns and a repetition time of 54.55 ns, which is derived according to the phase-time coding protocol used as thrice the interferometer delay.

The photon-number distribution of each pulse follows a resonator-specific temporal distribution and is not constant over the 5 ns time of the pump pulses. To lower the QBER, we only evaluate the 3 ns window on the late edge of each pulse, where the CAR is maximized because more photon pairs are produced than at the pulse's beginning.

We have previously implemented a postprocessing software described in [57]. It includes error correction and privacy amplification of the sifted key, which ultimately produces a secure key after each iteration of 90 s.

With this configuration, we performed QKD measurements with Alice and Bob connected directly to the source. Figure 9 shows the results of a key generation experiment over two hours, where, after each iteration, error correction takes place and a key is obtained. In this measurement, the QBER fluctuated in a range from 5.88% to 8.36% with an average of 7.16%. This fluctuation is caused by statistical effects due to the small sifted key rate. While the threshold for the generation of a secure key lies at around 11%, we were able to generate a secure key. However, a large portion of the sifted key had to be discarded during postprocessing. With a relatively high amount of error bits in the sifted key due to noise, numerous bits have to be published during error correction, and the key must be shrunk significantly during privacy amplification. This ultimately leads to the large difference between the sifted key rate with an average of 30.07 bit s^{-1} and the

actual secure key rate of 3.39 bit s^{-1} on average. Nevertheless, the usability of the chip as a photon-pair source for QKD was successfully demonstrated.

The key exchange ran for over 2 h without any instability in the locking of the resonator. Finally, the measurement was limited in time by a drift of the phase-QBER due to non-ideal temperature control of the interferometers with the large delays.

V. DISCUSSION AND OUTLOOK

Preceding our work, the creation of entangled photon-pairs in silicon or silicon-nitride waveguides on photonic chips was discussed in recent publications [5,60,61]. Resonators on chips to enhance the SFWM efficiency and create frequency combs of entangled photon pairs was successfully demonstrated [4,37,39,62]. Finally, the implementation of such photon-pair sources in QKD setups has been demonstrated [2]. In other setups, filters are incorporated on the PIC, but photon-pair production is performed in straight waveguides without resonators to enhance efficiency [63].

With the work presented here we extend and combine these approaches with a fully integrated photon-pair source on a photonic chip, which has all crucial filter elements directly on the chip and uses a PDH locking scheme for stable long-term photon-pair generation. Hence, the chip can serve as a fully integrated source of time-bin-entangled photon pairs, usable in time-bin variants of the BBM92 protocol.

Our setup focuses on the on-chip photon pair generation, both the pump laser and demultiplexing remain in external fiber-based setups. In principle, however, both could be implemented on chips as well, thereby enabling an all-in-one source. Our work marks an important step toward such a source by combining photon-pair generation and filter elements on a single chip.

A significant reduction of photons in the background from SRS with the on-chip filter elements was demonstrated. However, an unknown nonlinear effect near the pump light, covering the most important parts of the SFWM-spectrum, still leads to a low CAR.

While other publications also find a significant influence of SRS on CAR [5], a nonlinear noise effect with around 500 GHz width around the laser at 193.35 THz has only rarely been reported, and the root cause has not been identified [51–53]. The existence of this effect in our chip significantly undermines its usability as a pure photon-pair source. To resolve this issue, future investigations must be conducted to avoid this effect. Other possibilities to bypass the influence of the observed noise are using a chip material or waveguide geometry with significantly lower group-velocity dispersion. With this approach, the width of the SFWM spectrum will increase, and the photon pairs in the range of the noise will only make up a small portion of the whole. In addition to this, it is a general goal to increase the width of the SFWM phase matching to generate more available quantum channels in a QKD setup.

Besides the noise effect, the photon pairs emerged in a comb structure as expected, making them easily separable without disadvantageous effects at the channel fringes.

Our high-frequency implementation of the PDH-locking ensures high stability of the rings' resonance position. With a complete theoretical description of the pulsed PDH locking scheme, we were also able to find the optimal working conditions for the new mode of operation.

With this method, the source's stability is no longer limited by the much more unstable ring resonators within which a relatively large amount of energy is dispersed, but the ordinarily much more stable filtering units constitute the new limit. By switching those from rings to an AMZI series, it should be possible to increase their stability in future chip generations and reduce current requirements for temperature stabilization. Due to the cosine-like spectra of the AMZI compared to the narrow peaks of the triple-ring filters, small temperature-induced shifts in the filter spectra could be intercepted and readjusted more easily.

Finally, we successfully incorporated the chip into our QKD setup, which itself is not chip-based but a fiber-based setup, and generated secure keys for more than 2 h. Limitations in the QBER and key rate were set by the low CAR, mentioned above. Limitations in the long-term stability of the source were not given by the stability of the photon-pair generation itself, but due to thermal instabilities of the used high-delay interferometers. The trade-off between high-Q resonators with large decay times and high photon-pair generation rate, and lower Q factors and smaller interferometer delays should be further investigated.

Our chip source offers the possibility of supplying multiple parties simultaneously in a star-shaped QKD network. However, due to the spectral width of the unknown noise (cf. Sec. IV B) in combination with the small spectral width of the phase-matching of SFWM due to the high dispersion (cf. Sec. IV B), this is limited in the measurements we have shown. And even the performance of the frequency pairs with the best signal-to-noise ratio is less than in comparable setups from other publications [2,5,39].

In addition to the performance loss caused by noise on the chip, the overall QKD system could also achieve higher key rates by using DEMUX devices with lower losses or by using SNSPDs instead of Avalanche detectors.

VI. CONCLUSION

We have demonstrated a fully integrated on-chip photon-pair source with ring resonators of 50 GHz FSR and filtering units with 100 GHz implemented directly on the chip. It was shown that these could significantly reduce unwanted spectral components, especially due to their proximity to the resonators. For long-term stability over several hours of the micro-ring resonators on-chip, we implemented a high-frequency PDH-locking scheme, working at around 1.5 GHz. To stabilize the resonators even in pulsed operation, we developed a theoretical model to determine the optimum modulation frequency. This enables pulsed operation with a repetition rate of around 54 MHz and a pulse duration of 5 ns, suitable for QKD operation.

We integrated the photon-pair source successfully into our existing QKD setup and established its functionality in a two-party quantum key distribution. Even with the occurrence of unexpected single-photon noise close to our pump frequency

that covers about 500 GHz of the photon-pair spectrum and a QBER of approximately 7%, we were able to achieve secure key rates of 3.4 bit s^{-1} over 2 h, after error correction and privacy amplification.

ACKNOWLEDGMENTS

This research was funded by the Deutsche Forschungsgemeinschaft (DFG, German Research Foundation), under Grant No. SFB 1119–236615297. We thank Michael Kues from Leibniz University Hannover for valuable discussions and insights.

DATA AVAILABILITY

The data that support the findings of this article are publicly available [64].

APPENDIX: PDH SIGNAL CALCULATION

In analogy to the experiment, the PDH signal is calculated in three steps. First, the modulated light before the resonator is modeled. Then the reflection at the resonator is added. And lastly, the error signal is extracted.

The initial pump light consists of three parts. The base of the light is made up of a single-frequency planar wave, described by

$$E_0(t) = \exp(-\mathrm{i}\omega_0 t). \tag{A1}$$

This is then multiplied by the parts representing the amplitude $M_\mathrm{A}(t)$ and phase $M_\mathrm{P}(t)$ modulation. The amplitude modulation is represented by a real function periodic in the amplitude modulation frequency ω_AM and can thus be written as

$$\sum_{j=-\infty}^{\infty} a_j \mathrm{e}^{-\mathrm{i}j\omega_\mathrm{AM}t}. \tag{A2}$$

In a similar way, the phase modulation is represented by a sine with amplitude h and frequency ω_PM:

$$\varphi(t) = \varphi_0 + h\sin(\omega_\mathrm{PM}t + \varphi_1), \tag{A3}$$

$$M_\mathrm{P}(t) = \exp[-\mathrm{i}\varphi(t)]. \tag{A4}$$

With the Jakobi-Anger expansion [47] this term can be transformed:

$$M_\mathrm{P}(t) = \mathrm{e}^{-\mathrm{i}\varphi_0}\exp(-\mathrm{i}h\sin(\omega_\mathrm{PM}t + \varphi_1)) \tag{A5}$$

$$= \mathrm{e}^{-\mathrm{i}\varphi_0}\sum_{m=-\infty}^{\infty} J_m(h)\mathrm{e}^{-\mathrm{i}m(\omega_\mathrm{PM}t+\varphi_1)}. \tag{A6}$$

Here $J_m(h)$ is the mth Bessel function of the first kind. The modulated electric field is then described by

$$E_\mathrm{M}(t) = E_\mathrm{in}(t)M_\mathrm{A}(t)M_\mathrm{P}(t) \tag{A7}$$

$$= E_0\mathrm{e}^{-i(\omega_0 t+\varphi_0)}\sum_{m,j=-\infty}^{\infty} a_j b_m \mathrm{e}^{-\mathrm{i}(m\omega_\mathrm{PM}+j\omega_\mathrm{AM})t} \tag{A8}$$

with

$$b_m = J_m(h)\mathrm{e}^{-\mathrm{i}m\varphi_1}. \tag{A9}$$

In the next step, the reflection at the resonator is considered. This is performed in the frequency domain, as the frequency-dependent reflectivity of the microring is well known:

$$\tilde{F}(\omega, \Phi) = \frac{r - \exp[(-\mathrm{i}\omega n/c) - \alpha)2\pi R + \Phi]}{1 - r^*\exp[(-\mathrm{i}\omega n/c - \alpha)2\pi R + \Phi]}. \tag{A10}$$

Here ω is the frequency of the reflected light, Φ a variable phase within the ring, r the reflectivity of the input coupler, R the ring's radius, n the refractive index, and c the speed of light.

For further calculations, the E field is transformed into the frequency domain:

$$\tilde{E}(\omega) = \mathcal{F}\{E(t)\} \tag{A11}$$

$$= \frac{1}{\sqrt{2\pi}}\int_\mathbb{R} \mathrm{d}t\; E_0\mathrm{e}^{-i(\omega_0 t+\varphi_0)} \times \sum_{j,m=-\infty}^{\infty} a_j b_m \mathrm{e}^{-\mathrm{i}(m\omega_\mathrm{PM}+j\omega_\mathrm{AM})t+\mathrm{i}\omega t} \tag{A12}$$

$$= \sqrt{2\pi}E_0\mathrm{e}^{-\mathrm{i}\varphi}\sum_{j,m=-\infty}^{\infty} a_j b_m \times \delta(\omega - \omega_0 - m\omega_\mathrm{PM} - j\omega_\mathrm{AM}). \tag{A13}$$

The reflection is then modeled by multiplication with the frequency response function $\tilde{F}(\omega)$:

$$\tilde{E}_\mathrm{out}(\omega) = \tilde{F}(\omega)\sqrt{2\pi}E_0\mathrm{e}^{-\mathrm{i}\varphi} \times \sum_{j,m=-\infty}^{\infty} a_j b_m \delta(\omega - \omega_0 - m\omega_\mathrm{PM} - j\omega_\mathrm{AM}). \tag{A14}$$

We are now interested in the spectrum of the intensity $I_\mathrm{out}(t) = E_\mathrm{out}(t)E^*_\mathrm{out}(t)$. We apply the convolution theorem. Note that we have

$$\tilde{f}(\omega) = \mathcal{F}\{f(t)\} \quad \rightarrow \quad \mathcal{F}\{f^*(t)\} = \tilde{f}^*(-\omega). \tag{A15}$$

Therefore, we can write

$$\tilde{I}_\mathrm{out}(\omega) = \mathcal{F}\{I_\mathrm{out}(t)\} \tag{A16}$$

$$= \int_\mathbb{R} \mathrm{d}\nu\; \tilde{E}_\mathrm{out}(\nu)\tilde{E}^*_\mathrm{out}(\nu - \omega) \tag{A17}$$

$$= 2\pi|E_0|^2 \times \sum_{\substack{j,j'=-\infty\\ m,m'=-\infty}}^{\infty} a_j a^*_{j'} b_m b^*_{m'} \times \tilde{F}(\omega_0 + m\omega_\mathrm{PM} + j\omega_\mathrm{AM}) \times \tilde{F}^*(\omega_0 + m\omega_\mathrm{PM} + j\omega_\mathrm{AM} - \omega) \times \delta((m - m')\omega_\mathrm{PM} + (j - j')\omega_\mathrm{AM} - \omega). \tag{A18}$$

Note the relation

$$\tilde{I}_\mathrm{out}(-\omega) = \tilde{I}^*_\mathrm{out}(\omega). \tag{A19}$$

At this point, the mixing is applied by multiplication with $h\sin(\omega_\mathrm{PM}t + \phi)$ representing the signal produced by the

signal generator:

$$I_{\text{out}}(t) = \frac{1}{\sqrt{2\pi}} \int_{\mathbb{R}} \mathrm{d}\omega\, \tilde{I}_{\text{out}}(\omega) \mathrm{e}^{-\mathrm{i}\omega t}, \tag{A20}$$

$$I_{\text{mix}}(t) = h I_{\text{out}}(t) \sin(\omega_{\text{PM}} t + \phi), \tag{A21}$$

$$\tilde{I}_{\text{mix}}(\omega) = h \frac{1}{\sqrt{2\pi}} \int_{\mathbb{R}} \mathrm{d}t\, I_{\text{out}}(t) \sin(\omega_{\text{PM}} t + \phi) \mathrm{e}^{\mathrm{i}\omega t} \tag{A22}$$

$$= h \frac{1}{2} (\tilde{I}_{\text{out}}(\omega - \omega_{\text{PM}}) \mathrm{e}^{-\mathrm{i}\phi + \pi/2} - \tilde{I}_{\text{out}}(\omega + \omega_{\text{PM}}) \mathrm{e}^{\mathrm{i}\phi + \pi/2}). \tag{A23}$$

The DC component representing the error signal is given by

$$\tilde{I}_{\text{mix}}(0) = h \frac{1}{2} (\tilde{I}_{\text{out}}(-\omega_{\text{PM}}) \mathrm{e}^{-\mathrm{i}\phi + \pi/2} - \tilde{I}_{\text{out}}(\omega_{\text{PM}}) \mathrm{e}^{\mathrm{i}\phi + \pi/2}) \tag{A24}$$

$$= 2\pi |E_0|^2 h \sum_{\substack{j,j'=-\infty \\ m,m'=-\infty}}^{\infty} \mathrm{Im}\Big(a_j a_{j'}^* b_m b_{m'}^* \mathrm{e}^{\mathrm{i}\phi} \times \tilde{F}(\omega_0 + m\omega_{\text{PM}} + j\omega_{\text{AM}}) \times \tilde{F}^*[\omega_0 + (m-1)\omega_{\text{PM}} + j\omega_{\text{AM}}] \times \delta[(m - m' - 1)\omega_{\text{PM}} + (j - j')\omega_{\text{AM}}] \Big). \tag{A25}$$

[1] C. H. Bennett, G. Brassard, and N. D. Mermin, Quantum cryptography without Bell's theorem, Phys. Rev. Lett. **68**, 557 (1992).

[2] W. Wen, Z. Chen, L. Lu, W. Yan, W. Xue, P. Zhang, Y. Lu, S. Zhu, and X.-S. Ma, Realizing an entanglement-based multiuser quantum network with integrated photonics, Phys. Rev. Appl. **18**, 024059 (2022).

[3] P. Kok, W. J. Munro, K. Nemoto, T. C. Ralph, J. P. Dowling, and G. J. Milburn, Linear optical quantum computing with photonic qubits, Rev. Mod. Phys. **79**, 135 (2007).

[4] H. Mahmudlu, R. Johanning, A. van Rees, A. Khodadad Kashi, J. P. Epping, R. Haldar, K.-J. Boller, and M. Kues, Fully on-chip photonic turnkey quantum source for entangled qubit/qudit state generation, Nat. Photon. **17**, 518 (2023).

[5] F. Samara, A. Martin, C. Autebert, M. Karpov, T. J. Kippenberg, H. Zbinden, and R. Thew, High-rate photon pairs and sequential time-bin entanglement with Si_3N_4 microring resonators, Opt. Express **27**, 19309 (2019).

[6] N. Montaut, L. Sansoni, E. Meyer-Scott, R. Ricken, V. Quiring, H. Herrmann, and C. Silberhorn, High-efficiency plug-and-play source of heralded single photons, Phys. Rev. Appl. **8**, 024021 (2017).

[7] M. Tippmann, E. Fitzke, O. Nikiforov, P. Kleinpaß, T. Dolejsky, M. Mengler, and T. Walther, Fiber-based double-pass single-crystal photon-pair source for quantum key distribution in a network, Phys. Rev. Appl. **23**, 034017 (2025).

[8] S. Ramelow, A. Mech, M. Giustina, S. Gröblacher, W. Wieczorek, J. Beyer, A. Lita, B. Calkins, T. Gerrits, S. W. Nam, A. Zeilinger, and R. Ursin, Highly efficient heralding of entangled single photons, Opt. Express **21**, 6707 (2013).

[9] L. K. Shalm, E. Meyer-Scott, B. G. Christensen, P. Bierhorst, M. A. Wayne, M. J. Stevens, T. Gerrits, S. Glancy, D. R. Hamel, M. S. Allman, K. J. Coakley, S. D. Dyer, C. Hodge, A. E. Lita, V. B. Verma, C. Lambrocco, E. Tortorici, A. L. Migdall, Y. Zhang, D. R. Kumor, *et al.*, Strong loophole-free test of local realism, Phys. Rev. Lett. **115**, 250402 (2015).

[10] X. Zhang, Y. Zhang, C. Xiong, and B. J. Eggleton, Correlated photon pair generation in low-loss double-stripe silicon nitride waveguides, J. Opt. **18**, 074016 (2016).

[11] H. Wang, Q. Zeng, H. Ma, and Z. Yuan, Progress on chip-based spontaneous four-wave mixing quantum light sources, Adv. Devices Instrum. **5**, 0032 (2024).

[12] X. Zhang, B. A. Bell, A. Mahendra, C. Xiong, P. H. W. Leong, and B. J. Eggleton, Integrated silicon nitride time-bin entanglement circuits, Opt. Lett. **43**, 3469 (2018).

[13] A. Rahmouni, R. Wang, J. Li, X. Tang, T. Gerrits, O. Slattery, Q. Li, and L. Ma, Entangled photon pair generation in an integrated SiC platform, Light Sci. Appl. **13**, 110 (2024).

[14] T. J. Steiner, J. E. Castro, L. Chang, Q. Dang, W. Xie, J. Norman, J. E. Bowers, and G. Moody, Ultrabright entangled-photon-pair generation from an AlGaAs-on-insulator microring resonator, PRX Quantum **2**, 010337 (2021).

[15] Y.-R. Fan, C. Lyu, C.-Z. Yuan, G.-W. Deng, Z.-Y. Zhou, Y. Geng, H.-Z. Song, Y. Wang, Y.-F. Zhang, R.-B. Jin, *et al.*, Multi-wavelength quantum light sources on silicon nitride micro-ring chip, Laser Photonics Rev. **17**, 2300172 (2023).

[16] W. Luo, L. Cao, Y. Shi, L. Wan, H. Zhang, S. Li, G. Chen, Y. Li, S. Li, Y. Wang, S. Sun, M. F. Karim, H. Cai, L. C. Kwek, and A. Q. Liu, Recent progress in quantum photonic chips for quantum communication and internet, Light Sci. Appl. **12**, 175 (2023).

[17] J. Aldama, S. Sarmiento, L. Trigo Vidarte, S. Etcheverry, I. López Grande, L. Castelvero, A. Hinojosa, T. Beckerwerth, Y. Piétri, A. Rhouni, E. Diamanti, and V. Pruneri, Integrated InP-based transmitter for continuous-variable quantum key distribution, Opt. Express **33**, 8139 (2025).

[18] F. M. Soares, M. Baier, T. Gaertner, N. Grote, M. Moehrle, T. Beckerwerth, P. Runge, and M. Schell, InP-based foundry PICs for optical interconnects, Appl. Sci. **9**, 1588 (2019).

[19] J. J. G. M. van der Tol, Y. Jiao, L. Shen, A. Millan-Mejia, V. Pogoretskii, J. P. van Engelen, and M. K. Smit, Indium phosphide integrated photonics in membranes, IEEE J. Sel. Top. Quantum Electron. **24**, 1 (2018).

[20] J. Klamkin, H. Zhao, B. Song, Y. Liu, B. Isaac, S. Pinna, F. Sang, and L. Coldren, Indium phosphide photonic integrated circuits: Technology and applications, in *2018 IEEE BiCMOS and Compound Semiconductor Integrated Circuits and Technology Symposium (BCICTS)* (IEEE, Piscataway, NJ, 2018), pp. 8–13.

[21] Z. Wang, Z. Fang, Z. Liu, Y. Liang, J. Liu, J. Yu, T. Huang, Y. Zhou, H. Zhang, M. Wang, and Y. Cheng, On-chip arrayed waveguide grating fabricated on thin-film lithium niobate, Adv. Photonics Res. **5**, 2300228 (2024).

[22] A. Liu, L. Liao, Y. Chetrit, J. Basak, H. Nguyen, D. Rubin, and M. Paniccia, Wavelength division multiplexing based photonic integrated circuits on silicon-on-insulator platform, IEEE J. Sel. Top. Quantum Electron. **16**, 23 (2009).

[23] S.-Y. Ren, W.-Q. Wang, Y.-J. Cheng, L. Huang, B.-Z. Du, W. Zhao, G.-C. Guo, L.-T. Feng, W.-F. Zhang, and X.-F. Ren, Photonic-chip-based dense entanglement distribution, PhotoniX **4**, 12 (2023).

[24] T. Honjo, K. Inoue, and H. Takahashi, Differential-phase-shift quantum key distribution experiment with a planar light-wave circuit Mach–Zehnder interferometer, Opt. Lett. **29**, 2797 (2004).

[25] T. Inagaki, N. Matsuda, O. Tadanaga, M. Asobe, and H. Takesue, Entanglement distribution over 300 km of fiber, Opt. Express **21**, 23241 (2013).

[26] T. Honjo, S. W. Nam, H. Takesue, Q. Zhang, H. Kamada, Y. Nishida, O. Tadanaga, M. Asobe, B. Baek, R. Hadfield, S. Miki, M. Fujiwara, M. Sasaki, Z. Wang, K. Inoue, and Y. Yamamoto, Long-distance entanglement-based quantum key distribution over optical fiber, Opt. Express **16**, 19118 (2008).

[27] H. Shibata, T. Hiraki, T. Tsuchizawa, K. Yamada, Y. Tokura, and S. Matsuo, A waveguide-integrated superconducting nanowire single-photon detector with a spot-size converter on a Si photonics platform, Supercond. Sci. Technol. **32**, 034001 (2019).

[28] S. Ferrari, C. Schuck, and W. Pernice, Waveguide-integrated superconducting nanowire single-photon detectors, Nanophotonics **7**, 1725 (2017).

[29] J. A. Dolphin, T. K. Paraïso, H. Du, R. I. Woodward, D. G. Marangon, and A. J. Shields, A hybrid integrated quantum key distribution transceiver chip, npj Quantum Inf. **9**, 84 (2023).

[30] C. G. H. Roeloffzen, M. Hoekman, E. J. Klein, L. S. Wevers, R. B. Timens, D. Marchenko, D. Geskus, R. Dekker, A. Alippi, R. Grootjans, A. van Rees, R. M. Oldenbeuving, J. P. Epping, R. G. Heideman, K. Worhoff, A. Leinse, D. Geuzebroek, E. Schreuder, P. W. L. van Dijk, I. Visscher, *et al.*, Low-loss Si_3N_4 triplex optical waveguides: Technology and applications overview, IEEE J. Sel. Top. Quantum Electron. **24**, 1 (2018).

[31] A. Dhakal, P. Wuytens, A. Raza, N. Le Thomas, and R. Baets, Silicon nitride background in nanophotonic waveguide enhanced Raman spectroscopy, Materials **10**, 140 (2017).

[32] B. E. Little, S. T. Chu, H. A. Haus, J. Forese, and J.-P. Laine, Microring resonator channel dropping filters, J. Lightwave Technol. **15**, 998 (1997).

[33] J. Yang, Q. Zhou, F. Zhao, X. Jiang, B. Howley, M. Wang, and R. T. Chen, Characteristics of optical bandpass filters employing series-cascaded double-ring resonators, Opt. Commun. **228**, 91 (2003).

[34] C. Chaichuay, P. P. Yupapin, and P. Saeung, The serially coupled multiple ring resonator filters and Vernier effect, Optica Applicata **39**, 175 (2009).

[35] S. Darmawan and M. K. Chin, Critical coupling, oscillation, reflection, and transmission in optical waveguide-ring resonator systems, J. Opt. Soc. Am. B **23**, 834 (2006).

[36] Z. Yin, K. Sugiura, H. Takashima, R. Okamoto, F. Qiu, S. Yokoyama, and S. Takeuchi, Frequency correlated photon generation at telecom band using silicon nitride ring cavities, Opt. Express **29**, 4821 (2021).

[37] C. C. Tison, J. A. Steidle, M. L. Fanto, Z. Wang, N. A. Mogent, A. Rizzo, S. F. Preble, and P. M. Alsing, Path to increasing the coincidence efficiency of integrated resonant photon sources, Opt. Express **25**, 33088 (2017).

[38] K. Guo, X. Shi, J. Yang, Y. Ding, H. Ou, and Y. Zhao, Generation rate scaling: The quality factor optimazation of microring resonators for photon-pair sources, Photonics Res. **6**, 587 (2018).

[39] C. Wu, Y. Liu, X. Gu, X. Yu, Y. Kong, Y. Wang, X. Quiang, J. Wu, Z. Zhu, X. Yang, and P. Xu, Bright photon-pair source based on a silicon dual-Mach-Zehnder microring, Sci. China Phys. Mech. Astron. **63**, 220362 (2019).

[40] K. Garay-Palmett, Y. Jeronimo-Moreno, and A. B. U'Ren, Theory of cavity-enhanced spontaneous four wave mixing, Laser Phys. **23**, 015201 (2012).

[41] I. T. Union, Spectral grids for WDM applications: DWDM frequency grid (International Telecommunication Union, Geneva, 2020), https://www.itu.int/epublications/publication/itu-t-g-694-1-2020-10-spectral-grids-for-wdm-applications-dwdm-frequency-grid.

[42] R. W. P. Drever, J. L. Hall, F. V. Kowalski, J. Hough, G. M. Ford, A. J. Munley, and H. Ward, Laser phase and frequency stabilization using an optical resonator, Appl. Phys. B **31**, 97 (1983).

[43] E. D. Black, An introduction to Pound–Drever–Hall laser frequency stabilization, Am. J. Phys. **69**, 79 (2001).

[44] J. P. Chambers, High frequency Pound-Drever-Hall optical ring resonator sensing, Ph.D. thesis, Texas A&M University, 2007.

[45] T. Carmon, L. Yang, and K. Vahala, Dynamical thermal behavior and thermal self-stability of microcavities, Opt. Express **12**, 4742 (2004).

[46] A. Arbabi and L. L. Goddard, Dynamics of self-heating in microring resonators, IEEE Photonics J. **4**, 1702 (2012).

[47] A. Cuyt, V. B. Petersen, B. Verdonk, H. Waadeland, and W. B. Jones, *Handbook of Continued Fractions for Special functions* (Springer, Dordrecht, 2008).

[48] J. Liu, *Photonic Devices* (Cambridge University Press, Cambridge, 2009).

[49] W. Lee, P. Muñoz-Galindo, I. Hegeman, Y.-S. Yong, M. Dijkstra, S. M. García-Blanco, and H. L. Offerhaus, Study on multiple waveguide platforms for waveguide integrated Raman spectroscopy, OSA Continuum **3**, 1322 (2020).

[50] S. Gundavarapu, G. M. Brodnik, M. Puckett, T. Huffman, D. Bose, R. Behunin, J. Wu, T. Qiu, C. Pinho, N. Chauhan, J. Nohava, P. T. Rakich, K. D. Nelson, M. Salit, and D. J. Blumenthal, Sub-hertz fundamental linewidth photonic integrated Brillouin laser, Nat. Photon. **13**, 60 (2019).

[51] S. Clemmen, A. Perret, J. Safioui, W. Bogaerts, R. Baets, S.-P. Gorza, P. Emplit, and S. Massar, Low-power inelastic light scattering at small detunings in silicon wire waveguides at telecom wavelengths, J. Opt. Soc. Am. B **29**, 1977 (2012).

[52] L.-T. Feng, Y.-J. Cheng, X.-Z. Qi, Z.-Y. Zhou, M. Zhang, D.-X. Dai, G.-C. Guo, and X.-F. Ren, Entanglement generation using cryogenic integrated four-wave mixing, Optica **10**, 702 (2023).

[53] W. Wen, W. Yan, C. Lu, L. Lu, X. Wu, Y. Lu, S. Zhu, and X.-S. Ma, Polarization-entangled quantum frequency comb from a silicon nitride microring resonator, Phys. Rev. Appl. **20**, 064032 (2023).

[54] P. B. Coates, The correction for photon 'pile-up' in the measurement of radiative lifetimes, J. Phys. E **1**, 878 (1968).

[55] J. Rapp, Y. Ma, R. M. Dawson, and V. K. Goyal, Dead time compensation for high-flux depth imaging, in *ICASSP 2019-2019 IEEE International Conference on Acoustics, Speech and Signal Processing (ICASSP)* (IEEE, New York, 2019), pp. 7805–7809.

[56] E. Fitzke, A quantum hub for star-shaped quantum key distribution networks, Ph.D. thesis, Technische Universität Darmstadt, 2024.

[57] E. Fitzke, L. Bialowons, T. Dolejsky, M. Tippmann, O. Nikiforov, T. Walther, F. Wissel, and M. Gunkel, Scalable network for simultaneous pairwise quantum key distribution via entanglement-based time-bin coding, PRX Quantum **3**, 020341 (2022).

[58] J. Kaltwasser, J. Seip, E. Fitzke, M. Tippmann, and T. Walther, Reducing the number of single-photon detectors in quantum-key-distribution networks by time multiplexing, Phys. Rev. A **109**, 012618 (2024).

[59] T. Dolejsky, E. Fitzke, L. Bialowons, M. Tippmann, O. Nikiforov, and T. Walther, Flexible reconfigurable entanglement-based quantum key distribution network, Eur. Phys. J.: Spec. Top. **232**, 3553 (2023).

[60] C. Xiong, X. Zhang, A. Mahendra, J. He, D.-Y. Choi, C. J. Chae, D. Marpaung, A. Leinse, R. G. Heideman, M. Hoekman, C. G. H. Roeloffzen, R. M. Oldenbeuving, P. W. L. van Dijk, C. Taddei, P. H. W. Leong, and B. J. Eggleton, Compact and reconfigurable silicon nitride time-bin entanglement circuit, Optica **2**, 724 (2015).

[61] H. Takesue, K.-i. Harada, K. Tamaki, H. Fukuda, T. Tsuchizawa, T. Watanabe, K. Yamada, and S.-i. Itabashi, Long-distance entanglement-based quantum key distribution experiment using practical detectors, Opt. Express **18**, 16777 (2010).

[62] C. Wu, Y. Liu, Y. Wang, J. Ding, P. Zhu, S. Xue, X. Yu, Q. Zheng, M. Yu, A. Huang, X. Fu, X. Qiang, M. Deng, J. Wu, and P. Xu, Optimization of quantum light sources and four-wave mixing based on a reconfigurable silicon ring resonator, Opt. Express **30**, 9992 (2022).

[63] W. Shin, K. Kwon, D. Lee, and H. Shin, Suppression of external noise in on-chip photon-pair sources, J. Korean Phys. Soc. **85**, 476 (2024).

[64] M. Mengler, J. Kaltwasser, E. Fitzke, T. Hoffmann, and T. Walther, Fully integrated entangled photon-pair source on photonic chip for a wavelength-multiplexed multi-party quantum key distribution network, TUdatalib, 2025, https://doi.org/10.48328/tudatalib-1936.